We are IntechOpen, the world's leading publisher of Open Access books Built by scientists, for scientists

5,300
Open access books available

130,000
International authors and editors

155M
Downloads

Our authors are among the

154
Countries delivered to

TOP 1%
most cited scientists

12.2%
Contributors from top 500 universities

BOOK CITATION INDEX CLARIVATE ANALYTICS INDEXED

WEB OF SCIENCE™

Selection of our books indexed in the Book Citation Index in Web of Science™ Core Collection (BKCI)

Interested in publishing with us?
Contact book.department@intechopen.com

Laser Annealing as a Platform for Plasmonic Nanostructuring

Nikolaos Kalfagiannis,
Demosthenes C. Koutsogeorgis,
Elefterios Lidorikis and Panos Patsalas

Additional information is available at the end of the chapter

Abstract

Nanoconstruction of metals is a significant challenge for the future manufacturing of plasmonic devices. Such a technology requires the development of ultra-fast, high-throughput and low cost fabrication schemes. Laser processing can be considered as such and can potentially represent an unrivalled tool towards the anticipated arrival of modules based in metallic nanostructures, with an extra advantage: the ease of scalability. Specifically, laser nanostructuring of either thin metal films or ceramic/metal multilayers and composites can result on surface or subsurface plasmonic patterns, respectively, with many potential applications. In this chapter, the photo-thermal processes involved in surface and subsurface nanostructuring are discussed and processes to develop functional plasmonic nanostructures with pre-determined morphology are demonstrated. For the subsurface plasmonic conformations, the temperature gradients that are developed spatially across the metal/dielectric structure during the laser processing can be utilized. For the surface plasmonic nanoassembling, the ability to tune the laser's wavelength to either match the absorption spectral profile of the metal or to be resonant with the plasma oscillation frequency can be utilised, i.e. different optical absorption mechanisms that are size-selective can be probed. Both processes can serve as a platform for stimulating further progress towards the engineering of large-scale plasmonic devices.

Keywords: laser annealing, laser induce self-assembly, plasmonics, surface plasmon resonance, plasmonic nanoparticles

1. Introduction

Plasmonic nanoparticles have become an increasingly common research area as well as becoming a key component in many important applications, such as solar energy harvesting [1–6], chemical sensing via surface-enhanced spectroscopies [7, 8–14], cancer treatment [15, 16] and optical encoding of information [17–20] to name a few. The main reason behind their adaptability, to these and other prominent applications, is their unique optical properties that allow for the manipulation of light below the diffraction limit. Among metals, Au and Ag are considered more suitable for plasmonic nanoparticles (PNPs) due to their stability when formed into nanoparticles and their strong LSPR absorption bands in the visible region of the spectrum [21, 22]. Under irradiation, the free electrons in a PNP are driven by the alternating electric field and collectively oscillate at a resonant frequency in a phenomenon known as localized surface plasmon resonance (LSPR) [23–27]. The LSPR phenomenon induced in PNPs depends strongly on their composition, size, shape, geometrical distribution and on the refractive index of the employed dielectric environment [28–30]. To this end, efforts are undertaken in order to control these structural parameters depending on the growth conditions [22, 31–34].

A critical parameter in delivering practical plasmonic devices is the material preparation methods, which should allow the production of nanostructures with tunable plasmonic properties. So far, nanomaterials and nanodevice manufacturing have traditionally followed two distinct routes: (a) the top-down approach, where a process starts from a uniform material and subsequently finer and finer tools are employed to create smaller structures, like lithographic processes [35–37] and/or ion beam nanofabrication [38] and (b) the bottom-up approach, where smaller components of atomic or molecular dimensions self-assemble together, according to a natural physical principle or an externally applied driving force, to give rise to larger and more organized systems, like atomic layer deposition [39], cold welding [40], flash thermal annealing [41, 42], pattern transfer [43] and template stripping [44–46]. Practically, the top-down approach offers unequalled control and reproducibility down to a few nanometres in feature size but at high cost for large area manufacturing, while the bottom-up route applies for macroscopic scale nanopatterning albeit without the fine feature and reproducibility control.
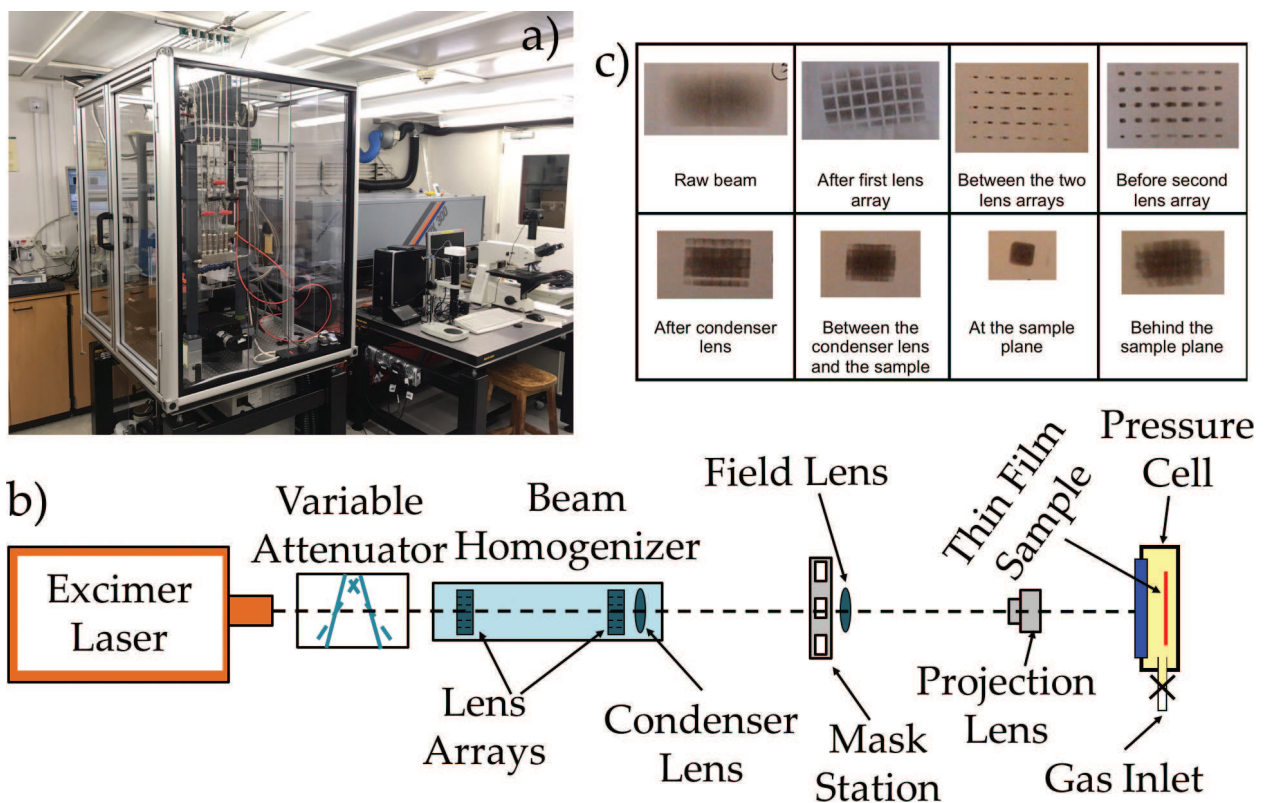
The use of laser radiation can be viewed as an intermediate route for nanotechnology manufacturing. Light-matter interactions offer precise energy delivery and control over the physicochemical processes in the nanoworld. Amongst the methodologies followed for creating nanoparticle arrangements and/or nanocomposite thin films, laser annealing (LA) has been proven to be simple and versatile, providing freedom of design, fast processing, compatibility with large-scale manufacturing and allowing for the use of inexpensive flexible substrates [17, 19, 47], due to the ultra-fast and macroscopically cold process. For example, LA of a thin metal film results into nanoparticle arrangements on top of a substrate [11, 13, 14, 47–54], while embedded nanoparticles in a dielectric matrix can be fabricated in large scale through the LA of a stack of alternating ultrathin layers of a metal and a dielectric [17, 18].

One of the key design issues in LA is the spatial distribution of the energy delivery (from the laser pulse) and the precise temporal temperature profile emerged in the structure (caused by

this energy). Understanding the dependence of the temperature profile on the nanoparticle/ substrate geometries can provide valuable insights in order to be able to design the appropriate LA process and get custom-made plasmonic devices. In the systems of interest, several effects such as material absorption, plasmon resonances and interference contribute to how the absorption is distributed, while the material thermal properties and the laser pulse profile determine the temperature transients developed. Here, the investigations required to extract the underline physical understanding of all these photothermal processes, involved in surface and sub-surface laser nanostructuring, are summarised.

2. UV laser annealing experimental set-up

A typical laser processing apparatus, such as the one used for the experimental part of the work that will be presented later, is shown in **Figure 1**. It comprises three main components: (i) the two laser sources, (ii) the laser beam delivery system and (iii) the sample manipulation stage.

Figure 1. (a) Digital photo of the laser annealing system at Nottingham Trent University, (b) schematic representation of the beam delivery path and (c) snapshots of the laser spot at different positions of the beam path.
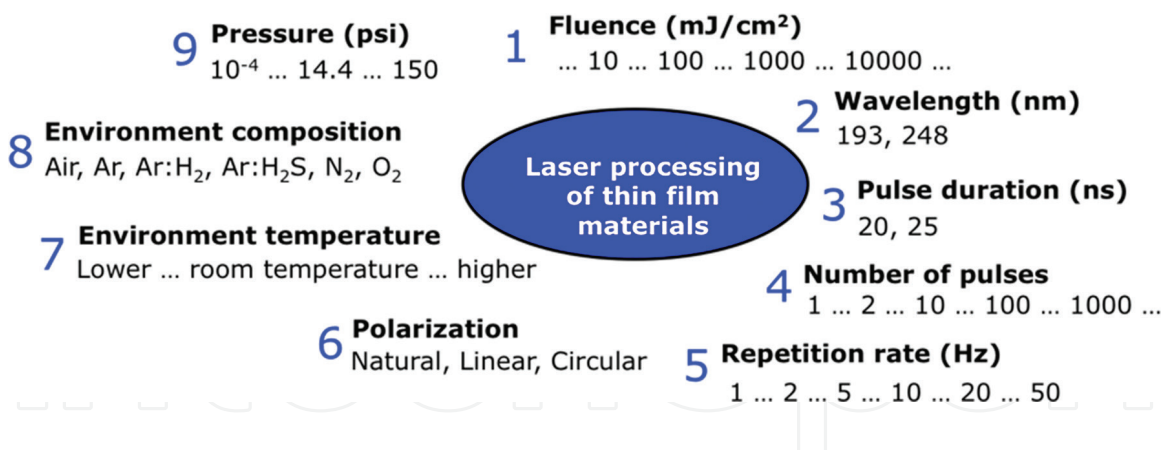
(i) The two laser sources are an excimer laser (LAMBDA PHYSIK LPX 305i) which is capable of providing unpolarized light pulses of 25 ns in duration and up to 1200 mJ/pulse at 248nm (KrF) and an excimer laser (LAMBDA PHYSIK LPX 205i) capable of providing unpolarized

light pulses of 20 ns up to 700 mJ/pulse at 193 nm (ArF). The raw beam, in both cases, is approximately 30×15 mm^2 with a Gaussian-like profile on the long axis and an almost top-hat profile on the short axis.

(ii) The beam delivery system is composed of a variable attenuator, a beam homogeniser and a mask-projection system. The variable attenuator employs a partially reflective first plate (angled at various positions) reflecting part of the laser beam and a second plate that compensates for the parallel displacement of the beam caused by the first plate. The attenuator has a variable throughput from 10% up to 90% of the original beam. The beam homogenizer (Exitech Ltd., type EX-HS-700D) employs two lens arrays and a condenser lens. The condenser lens provides a laser spot of pre-determined size (13×13 mm^2) at a certain distance with top-hat profiles on both axes (better than 2% uniformity). This homogenized beam coincides with a mask which is projected onto the sample via a combination of a field and projection lenses.

(iii) Finally, an X-Y-Z stage is in place in order to manipulate the sample and laser process different areas on it. The translational stage is operated via a controller with specialised software also being capable of externally triggering the laser. Thus, the whole operation is becoming fully automated. An appropriate mask and a ×5 objective lens set the laser spot delivered onto the samples to be a 2.5×2.5 mm^2 square spot.

The system has been designed in a way to be versatile and flexible, allowing for an extended degree of freedom of operation, thus providing the user with a wide spectrum of experimental parameters to vary from. These parameters are shown in **Figure 2**.

Figure 2. The nine experimental parameters of laser annealing system.

1. Fluence (mJ/cm^2): The fluence of the laser, i.e. the energy density delivered to the sample, is adjusted by the variable attenuator. The maximum fluence may also vary depending on the size of the mask and the objective lens used to project the laser spot onto the sample's surface and of course from the excimer laser source: KrF laser is capable of providing a raw beam of 1200 mJ/pulse, whereas the ArF is capable of providing a raw beam of 700 mJ/pulse. Regarding the spot size, this is defined by the appropriate masks, on the mask station and the combination of field and projection lenses.

2. Wavelength (nm): The KrF laser emits light at 248 nm, while the ArF emits light deeper in the UV spectral range; at 193 nm. At this deep UV wavelength, most of the energy is absorbed by O_2 molecules in the air, which are then turned into ozone. To avoid the energy losses and thus the minimisation of the energy throughout the process in addition to avoiding health hazards due to the toxicity of ozone, the beam delivery path of the ArF laser is enclosed in sealed tubes, to allow for N_2 flow during the laser process.

3. Pulse duration (ns): Both excimer lasers are ultra-short pulsed UV lasers. The KrF has a pulse width of 25 ns, while the ArF has a pulse width of 20 ns.

4. Number of pulses: The applied number of pulses to the sample.

5. Repetition rate (Hz): The repetition rate is externally controlled and may vary from 1 to 50 Hz for both laser sources.

6. Polarization: While an excimer laser is usually producing completely randomly polarized light an optical filter that passes light of a specific polarization (polariser) may be used to block waves of other polarizations and convert a beam of light of undefined or mixed polarization into a beam with well-defined polarization state.

7. Environment temperature: The home-built system has the capability to have the sample sitting at −196°C (liquid nitrogen) or heated at elevated temperatures during the LA process.

8. Environment composition: The pressure cell, where the sample sits (shown in **Figure 1**), is supplied by a series of gases through appropriate pipelines connected to the cell. These gases are Ar, Ar:H_2, Ar:H_2S, N_2, and O_2. Depending on the application, the LA experiment may need to be conducted in an inert atmosphere (e.g., avoiding any oxidation occurring during the LA in air) or in a reacting atmosphere, where doping of the processed sample is seen necessary.

9. Pressure: In certain cases, low vacuum or high pressure application during LA (of any gaseous environment) is considered advantageous to avoid detrimental effects of ablation [17].
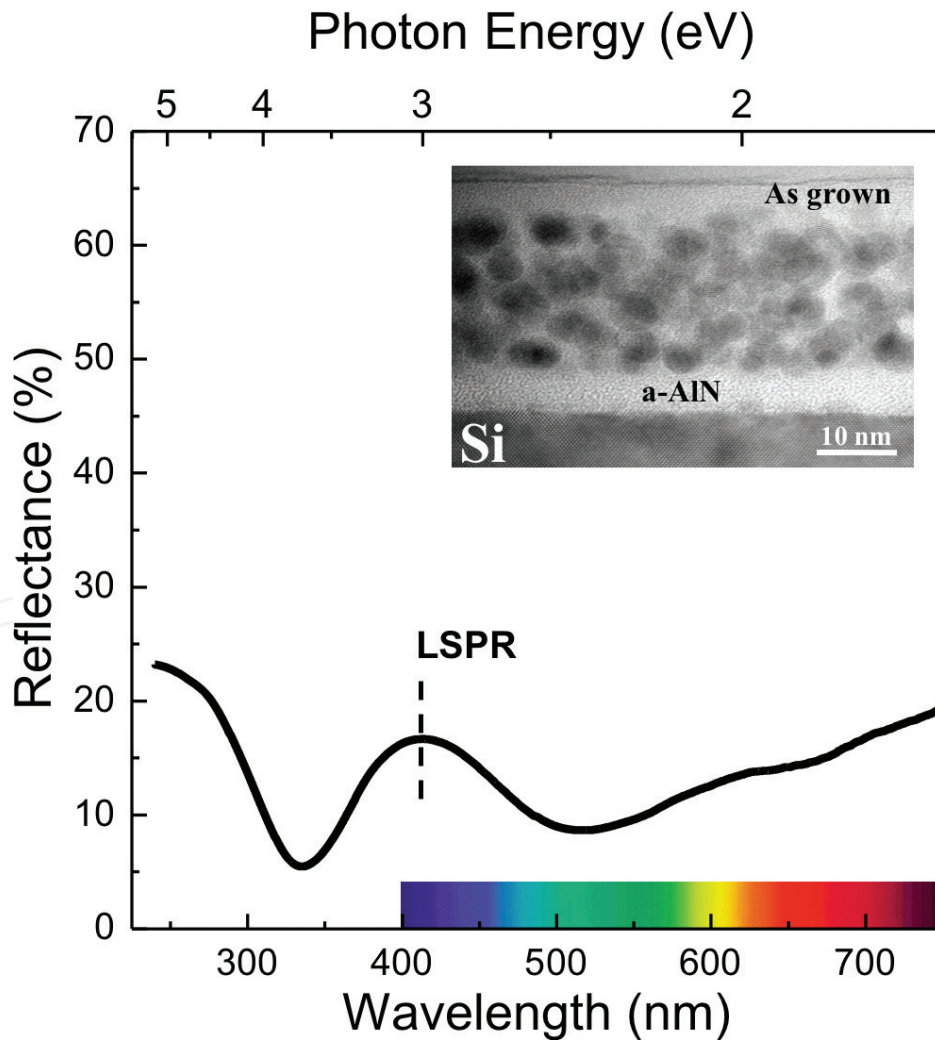
3. Sub-surface nanostructuring

3.1. Pulsed laser deposited nanocomposite AlN:Ag films

A robust nanoconstruction consisting of a narrow size distribution of PNPs embedded into a ceramic dielectric matrix emerges as the ideal configuration for applications such as authentication patterns and optical recording media specified for extreme conditions. To this end, AlN is an excellent candidate as a host matrix for PNPs due to its optical transparency, chemical inactivity, refractory character and high hardness. Ag is a characteristic example of noble metal that exhibits the strongest LSPR when formed into nanoparticles. However, silver's high diffusivity on one hand and the high melting point of AlN on the other hand

makes the fabrication of AlN:Ag(PNPs) nanocomposites an unfeasible task: Ag is either out-diffused to the surface (upon thermal treatment) or is atomically dissolved into AlN during growth [55]. Such obstacles prevented the extended use of AlN in plasmonics. Herein, strategies for the successful growth of AlN:Ag(PNPs) films by LA-based micropatterning are discussed.

3.1.1. Growth and processing of materials

AlN:Ag nanocomposite films (70–100 nm thick) were grown on n-type c-Si(100) wafers *via* pulsed laser deposition (PLD) in an in-house-built high-vacuum system ($P_b < 5 \times 10^{-8}$ mbar) using the third harmonic of a Nd:YAG laser (6 ns pulse duration, fluence 30 J/cm² at 10 Hz repetition rate). More details on sample preparation can be found elsewhere [19, 20]. The resulting nanocomposite films consisted of an amorphous AlN matrix with embedded pure Ag nanospheres, as displayed in the transmission electron microscopy (TEM) image in the inset of **Figure 3**. The embedded nanospheres exhibited LSPR, spectrally located at around 420 nm [20].

Figure 3. Optical reflectivity of AlN:Ag: as grown film. Inset depicts a cross section TEM image of the sample.
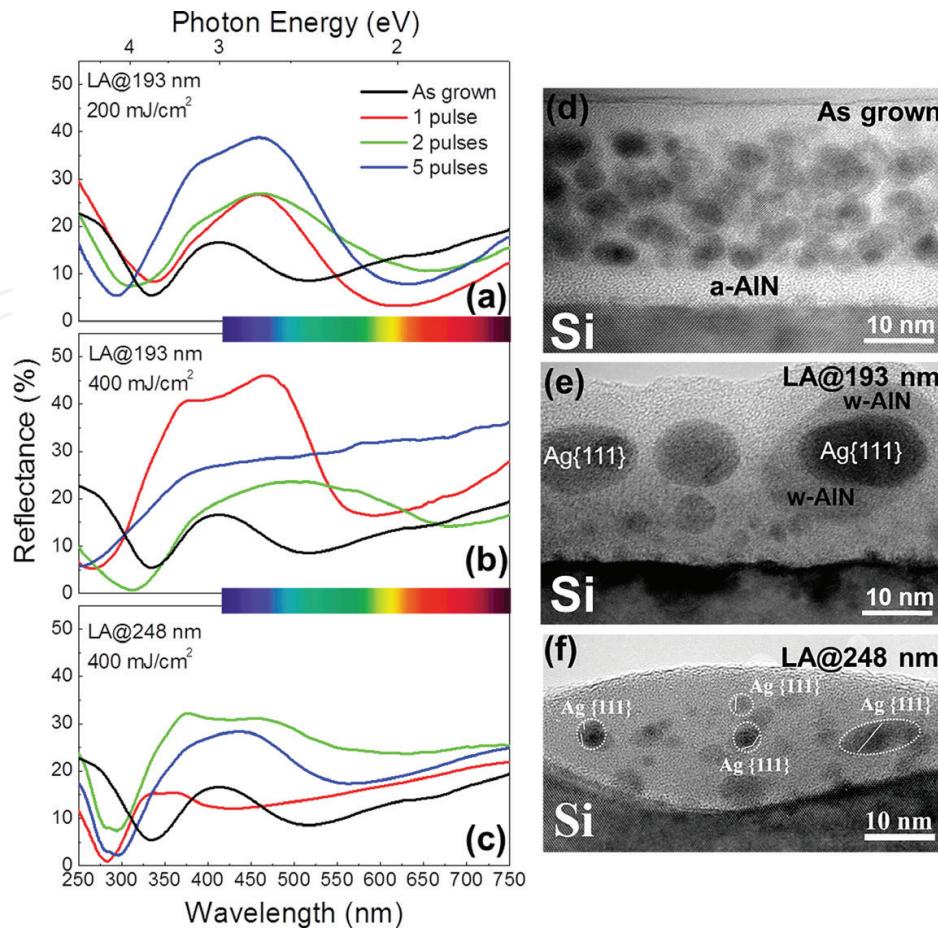
3.1.2. Laser processing

3.1.2.1. The effect of number of pulses

AlN:Ag films were processed with 1, 2 or 5 pulses at 200 mJ/cm^2 and 400 mJ/cm^2, i.e. just above the annealing threshold and just below the ablation threshold at 193 and 248 nm laser wavelengths. The pulse repetition rate in any case was 1 Hz, eliminating any possibility for transient thermal phenomena and thus allowing for each successive pulse to interact with a perfectly relaxed AlN:Ag film at room temperature. The optical reflectivity spectra are presented in **Figure 4**. In the case of the 193 nm wavelength at low fluence (200 mJ/cm^2) (**Figure 4a**), each successive pulse leads to a cumulative LSPR enhancement, in terms of the integral strength of the LSPR band, indicating that Ag diffusion results in shape and size improvement of the plasmonic nanoparticles; the Si substrate's E1 critical point at around 350 nm [56] is also gradually emerging with the number of pulses due to the film's transparency, because of the crystallization of AlN as we will discuss in more detail in the following paragraphs. On the contrary, at high fluence (400 mJ/cm^2) (**Figure 4b**), the evolution of the reflectivity spectra with the number of laser pulses exhibits severe changes. The effect of one pulse at 400 mJ/cm^2 to the plasmonic response is more pronounced compared to that of five pulses at 200 mJ/cm^2, indicating that the structural modifications taking place during the 193 nm LA process are better associated with the laser fluence than with the total laser energy delivered. This will be further examined in the next section where the effect of laser fluence is discussed. For two applied pulses, the LSPR band is substantially broader indicating an exceptionally broad size distribution of Ag nanoparticles that can only be explained by means of Ag outdiffusion. Finally, for five pulses the reflectivity spectrum is characteristic of a homogeneous Ag layer on top of the AlN:Ag film indicating that none of the remaining Ag is in the nanoparticle form.

3.1.2.2. The effect of laser wavelength

A major factor affecting the LA process is the laser wavelength, due to the different absorption coefficient of the amorphous AlN matrix and Ag. In the case of LA of AlN:Ag, using the 248 nm wavelength and fluence of 400 mJ/cm^2, the picture is quite more complex. At the first laser pulse (**Figure 4c**, red solid line), the pre-existing LSPR band is eliminated, possibly by dissolving of overheated, unstable Ag PNPs, whose constituent Ag atoms do not have the required diffusion time to reform into bigger Ag particles. Bigger particles, however, are observed after the second pulse resulting in intense LSPR peak (**Figure 4c**, green solid line). The lower photon energy at 248 nm and the fact that the pulse duration is shorter than the time required for Ostwald ripening in a cold environment [57, 58] (the process is indeed relatively cold because the 248 nm beam is not absorbed by the AlN matrix due to its high fundamental gap) allows for the Ostwald ripening process to take place in two steps: dissolution of particles for the first pulse and reforming of bigger particles close to the surface for the second pulse. Finally, the optical reflectivity spectrum for five pulses (**Figure 4c**, blue solid line) exhibits a broad LSPR band, resembling the broadening of the LSPR band for two applied pulses at 193 nm (**Figure 4b**, green solid line), but blue-shifted compared to the band for two pulses of 193 nm indicating a surrounding medium that is less optically dense than AlN (e.g. outdiffused Ag nanoparticles in air) [20].
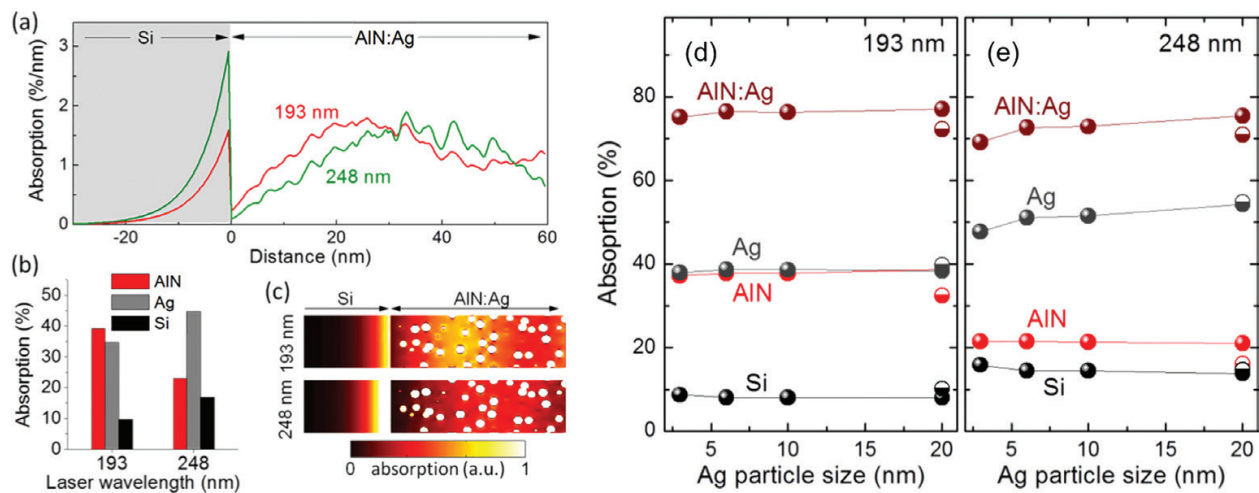
Figure 4. Optical reflectivity spectra for 1, 2 and 5 successive pulses for laser annealing using: (a) 193 nm wavelength, 200 mJ/cm² fluence, (b) 193 nm wavelength, 400 mJ/cm² fluence and (c) 248 nm wavelength, 400 mJ/cm² fluence. In all cases the black solid line, represents the as deposited film's optical response, which is shown for comparison. Cross-section TEM images of AlN:Ag/Si: (d) as-grown, (e) laser annealed with one pulse of 193 nm/400 mJ/cm² and (f) laser annealed with two pulses of 248 nm/400 mJ/cm².

Cross-sectional TEM images of the as-grown AlN:Ag and laser-treated areas (**Figure 4d–f**) reveal significant structural modifications for both wavelengths. The untreated films (**Figure 4d**) give no trace of crystalline AlN [59]. LA at 193 nm (**Figure 4e**) leads to agglomeration of Ag nanoparticles and formation of larger nanoparticles close to the surface of the film. This enlargement of Ag nanoparticles can be described as an Ostwald ripening phenomenon. Another important aspect of the 193 nm LA process is the partial crystallization of AlN into the wurtzite structure (w-AlN) around the enlarged nanoparticles (**Figure 4e**). Similar results occur after the 248 nm LA treatment (**Figure 4f**), although to a lesser extent due to the lower delivered photon energy, which is below the AlN's fundamental gap (6.2 eV). As a result, the laser beam interacts solely with the Ag nanoparticles. Consequently, the delivered energy to the substrate is higher than in the case of 193 nm LA, and thus the AlN/Si interface is significantly damaged. By the same token, the crystallization of the matrix is less likely to occur due to the lower effective temperature rise during the LA process.

To get an insight into the light absorption dynamics inside the film during LA, finite-difference time-domain (FDTD) simulations of a 60 nm thick nanostructured AlN:Ag film were

performed, where Ag consists of 3 nm diameter inclusions at 15% volume filling ratio randomly distributed inside the AlN matrix [20]. Laser light, for both wavelengths (193 nm and/ or 248 nm), is normally incident on the AlN:Ag film. Partially, it is absorbed by the film; partially, it is reflected and the rest is absorbed by the Si substrate. **Figure 5a** presents the absorption percentage per nm of length for the two wavelengths, where several configurations of randomly distributed Ag nanoparticles were averaged. The difference in the total film absorption, between the 193 and the 248 nm wavelengths, is small, with the 193 nm illumination being slightly more absorbed. The different standing wave patterns within the 60 nm film are also evident. Of great significance is the distribution of the absorbed light power among the different materials (**Figure 5b**). Considering that the Ag PNPs are dispersed at only 15% by volume, it is evident that they are the stronger absorbers in both cases. However, there is a significant deviation between the two annealing wavelengths: for 193 nm, a much more balanced absorption between AlN and Ag occurs, with minimal light energy reaching the Si substrate. In contrast, for 248 nm, most of the absorption occurs within the Ag inclusions, while at the same time, more light energy finds its way to the Si substrate causing significant damage. The absorption distribution maps for these two cases are shown in **Figure 5c**, considering a slice of one of the different randomized configurations. The fact that Ag nanoparticles act as absorption centres explains why AlN crystallization occurs only within a few nanometres from the nanoparticles surface. In addition, the more balanced absorption distribution in the film, as well as the minimal absorption by the Si substrate, qualitatively explains the superior annealing performance at 193 nm.

Figure 5. (a) Absorption distribution for a 60 nm thick AlN:Ag(15%vol)/Si film. (b) Absorption percentages for each constituent material within the AlN:Ag/Si structure. (c) Colour coded absorption distribution maps. (d) Absorption percentage within each material as a function of nanoparticle size, for 193 nm laser annealing wavelength and (e) Absorption percentage within each material as a function of nanoparticle size, for 248 nm laser annealing wavelength. The semi-open circles at 20 nm correspond to the nanoparticles having a non-absorbing 2.5 nm crystalline AlN ($n = 2.1$) layer around them.

Figures 5d and **5e** displays the cumulative absorption in each different material as a function of Ag particle size for the two annealing wavelengths. Ordered Ag NP arrays are considered here only for simplicity. Evidently, the 193 nm laser exhibits superior performance: unfluc-

tuating performance for all particle sizes, more balanced absorption between matrix and inclusions, slightly stronger overall film absorption and less substrate absorption. Semi-open circles at 20 nm correspond to the nanoparticles having a non-absorbing 2.5 nm crystalline AlN ($n = 2.1$) shell. This results in a small decrease in the matrix absorption due to the higher fundamental energy gap of w-AlN. The effect of shell creation thus is towards the direction of limiting the film's overall absorption, although it does not seem to be large enough to qualify as a self-limiting factor for the annealing process.
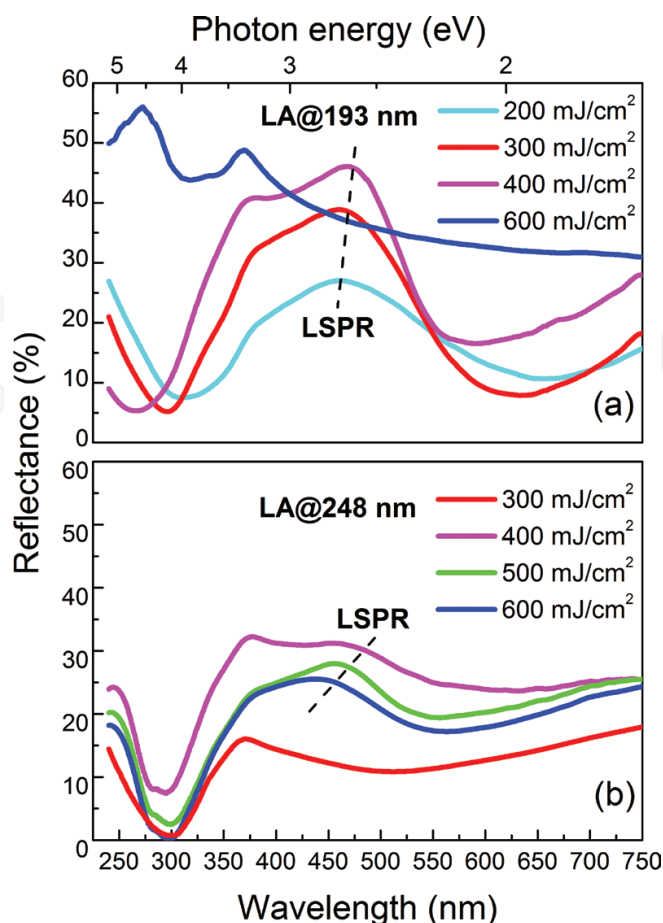
3.1.2.3. The effect of laser fluence

The data presented in **Figure 5** demonstrate that the laser fluence is an essential parameter for the LA process. The optical reflectivity spectra of the laser annealed AlN:Ag vs. the laser fluence for both processing wavelengths and the corresponding quantitative results are presented in **Figure 6**. Increasing the fluence of the 193 nm wavelength, from 200 to 400 mJ/cm^2, induces a spectral shift concomitantly with a significant enhancement of plasmon resonance. Both effects are respectively associated with changes of the matrix's refractive index and the Ag nanoparticles size. The laser fluence decreased the bandwidth (full width at half maximum of the fitted LSPR band), indicating a narrower size distribution of Ag nanoparticles due to the matrix crystallization, as well as to Ag particle enlargement causing weaker electronic confinement. Eventually, at higher fluence (e.g. 600 mJ/cm^2), the reflectivity spectrum reveals the Si features, indicating that this fluence exceeds the ablation threshold.

On the other hand, for LA using two pulses at 248 nm, the picture is quite different (**Figure 6b**). At 300 mJ/cm^2, the reflectivity spectrum is similar to the one pulse at 248 nm and 400 mJ/cm^2 (**Figure 4c**), which is characterized by the absence of LSPR, indicating that the provided energy is not enough to cause ripening of Ag and only dissolution is observed. For fluences exceeding 400 mJ/cm^2, a consistent LSPR blue shift is observed due to only a possible reduction of the refractive index of the surrounding medium, supporting the Ag outdiffusion to the free surface and the formation of Ag nanoparticles surrounded by air.

3.1.3. Application in optical encoding of information

The combination of structural modifications and the variation of AlN:Ag plasmonic response, introduced by LA, produces strong reflectivity contrast, which has been exploited to encode spectrally sensitive patterns [19, 20]. Patterns such as 'ALN:AG', 'ALN', and 'AL' have been produced by LA onto films of AlN:Ag, AlN and Al, respectively, deposited either on Si or sapphire substrates, using either the 193 nm or the 248 nm beam, and their response (in transmittance and reflectance) to different light colours was investigated using optical microscopy [19, 20]. The reflectivity contrast $\Delta R(=R_{LA}-R_{untreated})$ between treated and untreated areas of an AlN:Ag sample demonstrates the level of contrast the human eye can resolve; the spectral variations of such ΔR contrasts for 193 and 248 nm LA are presented in **Figure 7b** for all cases of laser treated AlN:Ag deposited on opaque Si substrates. Depending on the processing wavelength and LA conditions exceptional flexibility in selecting the required encoding ΔR contrast over the whole visible spectral range can exist. In particular, the spectral selectivity
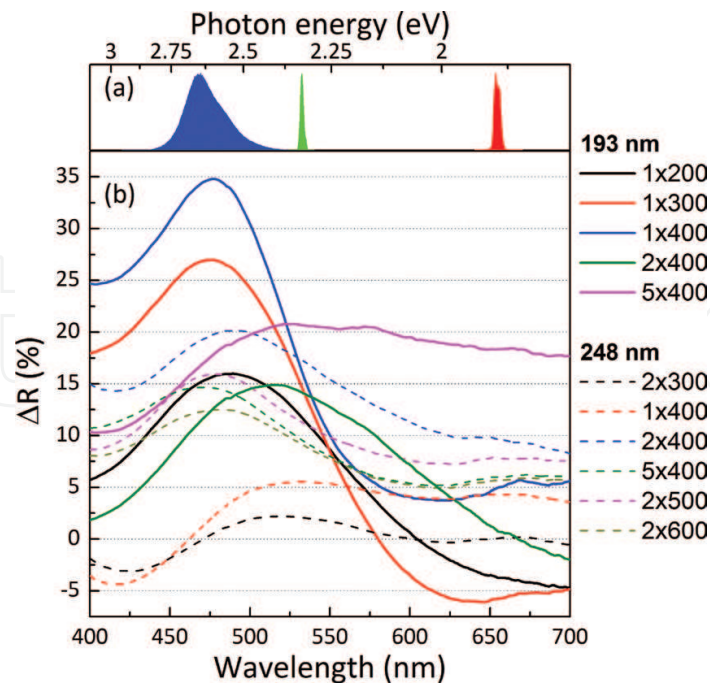
Figure 6. Optical reflectivity spectra with respect to laser fluence for LA at (a) 1 pulse at 193 nm and (b) 2 pulses at 248 nm.

is greater when large variations of ΔR are manifested in the visible spectrum. For example, for LA using one pulse of 400 mJ/cm² of 193 nm (**Figure 7b**, solid blue line), the ΔR ranges from 5% for red (650 nm) to 35% for blue (475 nm) providing very high spectral selectivity. These conditions are ideal for spectrally sensitive overt encoding. On the contrary, covert encoding requires more subtle spectral contrast ΔR in order for the pattern to be invisible under white light illumination and be revealed only under specific coloured illumination near the LSPR region. This can be done by, e.g., LA using two pulses of 500 mJ/cm² of 248 nm (**Figure 7b**, dashed magenta line).
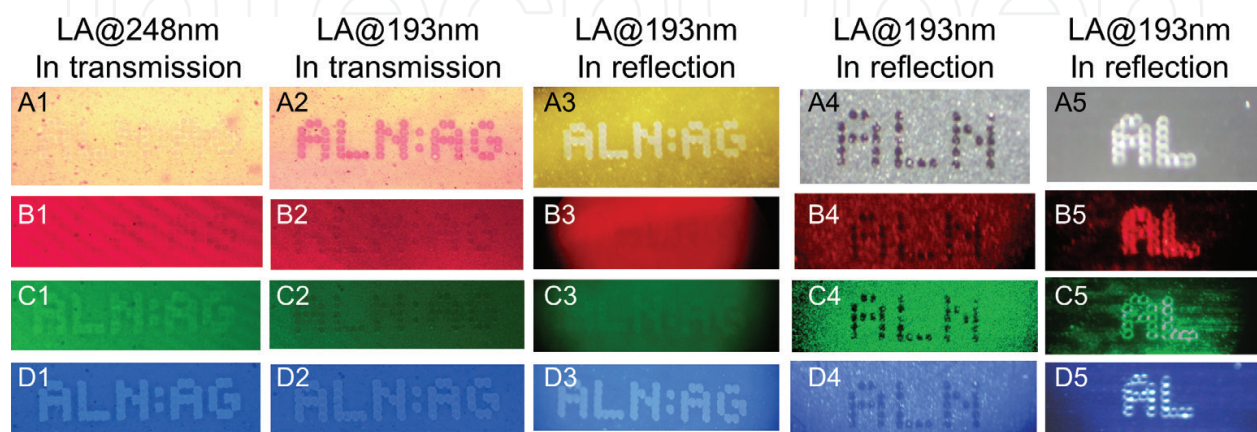
The potential of plasmonic encoding has been better demonstrated by optical microscopy images, where the sample is illuminated by different coloured light (blue/468 nm, green/532 nm, red/655 nm) [20]. For this demonstration, AlN:Ag, AlN and Al films were grown on sapphire substrates in order to evaluate both the reflection and transmission reading [20]; the relevant optical microscopy images are presented in **Figure 8**. Images A1-D1 demonstrate covert encoding in transmission reading, facilitated by LA of an AlN:Ag film at 248 nm. The pattern, with a pixel size of 60 μm, is almost invisible under white light illumination (A1) and is fully uncovered only under blue illumination (D1) where the LSPR is manifested. Images A2-D2

Figure 7. (a) Emission spectra of the three red-green-blue (RGB) light sources used for optical microscopy observations. (b) Spectral reflectivity contrasts (ΔR) for laser annealing of AlN:Ag on Si (opaque substrate) at 193 and 248 nm (purple and magenta lines, respectively) for various number of pulses and fluences demonstrating the flexibility in selecting the required encoding contrast.

and A3-D3 correspond to overt encoding in both transmission and reflection reading, realized by LA at 193 nm. The spectral sensitivity of the plasmonic patterns (A1-D1, A2-D2, A3-D3) contrasts the behaviour of patterns encoded by laser ablation in AlN (images A4-D4) and in Al (images A5-D5), which do exhibit similar contrasts for all colours, mostly due to scattering of light at the pixel edges. In addition to photosensitivity, AlN:Ag(PNPs) films have a unique combination of assets such as being harder than steel [20], chemically resistant against organic solvents [19, 20], almost having pitchless surface [19, 20] and are resistant to temperatures up to 600°C [20, 60].

Figure 8. Optical microscopy images of AlN:Ag, AlN, Al on sapphire using A. white, B. red, C. Green and D. blue illumination, in transmission (1, 2) or reflection (3–5) mode on sapphire for 248 nm (1), and 193 nm (2–5) laser annealing, respectively [20].

3.2. Magnetron sputtered AlN/Ag multilayer thin films

In this section, an alternative pathway is demonstrated, namely, starting from non-plasmonic metal/dielectric multilayers, which are then transformed into plasmonic templates by single-shot UV LA leading to a subsurface nanoconstruction involving plasmonic Ag nanoparticles embedded in a hard and inert dielectric matrix. The subsurface encapsulation of Ag nanoparticles provides durability and long-term stability. The morphology of the final composite film depends primarily on the nanocrystalline character of the dielectric host and its thermal conductivity. The emergence of LSPR and its adjustability, depending on the applied fluence, is demonstrated.

3.2.1. Growth and processing of materials

Multilayers consisting of alternate thin layers of AlN and Ag were fabricated in an in-house built high vacuum system (base pressure 2×10^{-6} Pa) employing the reactive magnetron sputtering technique. The AlN crystal structure was varied in the two sets of AlN/Ag by applying two different power values to the Al target, 100 and 15 W. This variation lead to different categories of sputtered AlN [46]: at 100 W high crystalline wurtzite AlN (w-AlN) was obtained while at 15 W an amorphous AlN (a-AlN) was obtained. The produced samples were subjected to LA with an excimer ArF source. The effect of a single-pulse LA step onto the structural and optical properties was investigated as a function of fluence (400–700 mJ/cm²) in an ambient atmosphere.
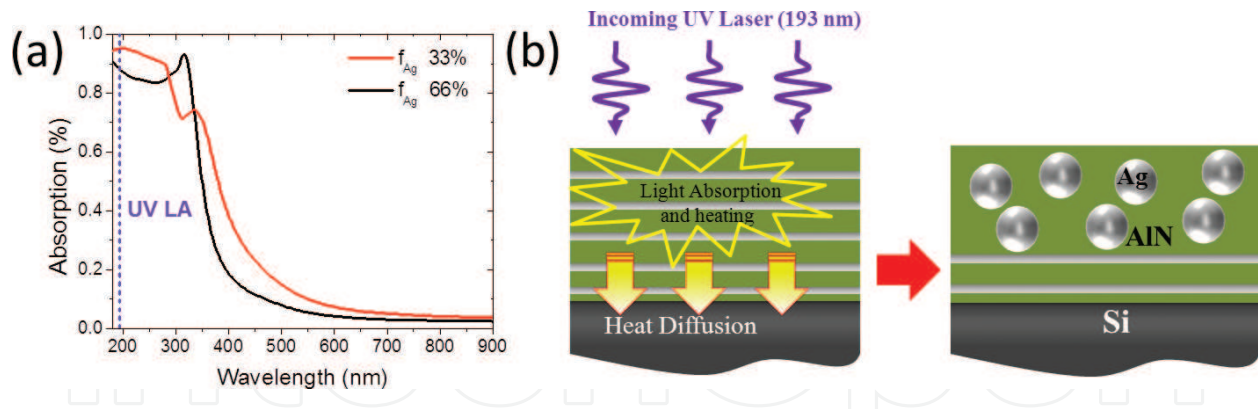
3.2.2. Laser processing

The heating dynamics involved in the multilayer structures during UV LA can be simulated/predicted performing optical and heat transport calculations. UV light propagation was solved via the FDTD method [61, 62], and a detailed map of the absorption profile in the multilayer and the substrate was obtained. The model system consists of a stratified multilayer structure of alternative dielectric (AlN) and metal layers (Ag) on a Si substrate, capped by AlN. The optical response of such a multilayer show high UV absorption (**Figure 9a**) due to silver's inter-band transitions at this spectral range. Under the proper experimental conditions, this high UV absorption was utilized to locally melt the structure. Due to the immiscibility of Ag with AlN, Ag diffusion will drive its transformation into a plasmonic nanocomposite with metallic PNPs embedded in a dielectric matrix (**Figure 9b**). The morphology of the nanocomposite and its optical response can be tuned by choosing materials and LA parameters such as: the nanocrystaline character of the dielectric which is strongly related to its thermal conductivity, the metal volume ratio and the total thickness of the multilayer.

The spatial absorption profile is convoluted with the temporal pulse profile (shown in **Figure 11b**, inset) and solved in the 1D heat transport equation [63]:

$$c(z)\rho(z)\partial_T T(z, t) = \partial_z \left[k(z)\partial_z T(z, t) \right] + Q(z, t) \tag{1}$$

where ∂_T, ∂_z denote partial derivatives with respect to time (t) and distance (z) from the top surface, respectively, and $Q(z, t) = \alpha(z)\,\varphi(t)$ is the laser heating source term defined by the product of the absorption spatial profile $\alpha(z)$ and the laser pulse temporal profile $\phi(t)$, with the total laser fluence given by:
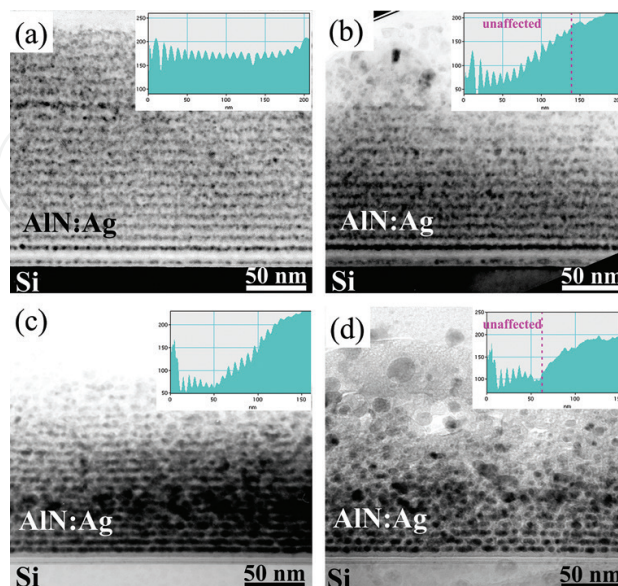
$$f = \int_{-\infty}^{\infty} \varphi(t)dt \tag{2}$$

Figure 9. (a) Spectral absorption of a stratified metal (Ag) dielectric (AlN) structure illustrated in (b) for two metal volume ratios 33 and 66%. The high UV absorption can be utilized for the further modification of the nanocomposite. (b) Schematic illustration of the laser treatment of the multilayer structure. Under UV laser radiation, the absorbed energy is converted into heat, which is diffused by thermal conduction into the Si substrate. The result of the laser treatment is to totally transform the multilayer structure into a nanocomposite of embedded plasmonic metallic NPs inside a dielectric matrix.

c, ρ and k are the specific heat capacity, the mass density and the thermal conductivity, respectively. These three terms have a spatial dependence due to the interchange of different materials. Eq. (1) is time-integrated numerically (by a 4th order Runge-Kutta scheme) in order to calculate the explicit temperature transient. To do that, we assume that: (i) electronic and lattice temperatures are in equilibrium, (ii) radiation and convection losses are negligible, (iii) material properties (absorption, heat capacity, mass density and thermal conductivity) remain constant during heating.
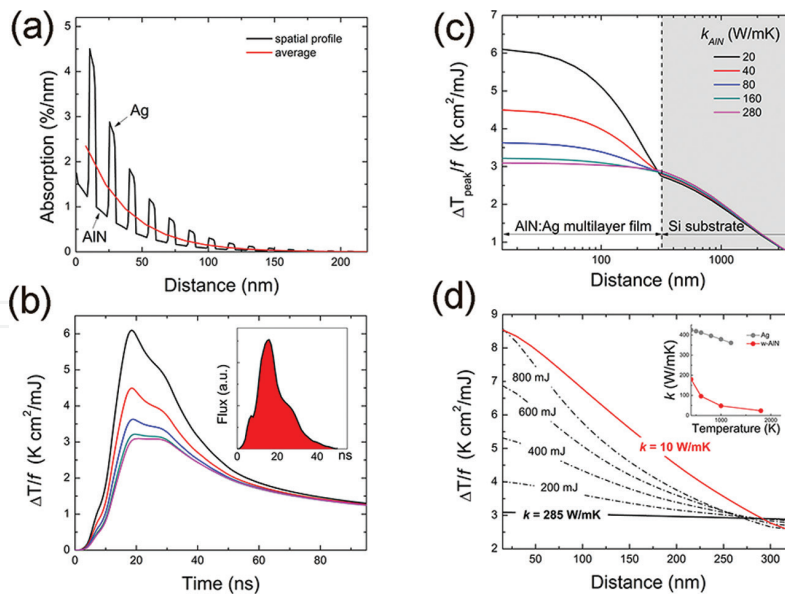
Relevant recent experiments of a single UV laser annealing (LA) on a ceramic/metal (in particular AlN/Ag) multilayer film are discussed [17]. This LA step is capable of driving the sub-surface modification of the metallic multilayers resulting into LSPR behaviour from PNPs that are formed and dispersed in a depth of several nanometre away from the surface. TEM observations from the as-deposited samples (**Figure 10a** and **b**) verified their multilayer character.

Figure 10. TEM cross sectional images of: (a) the as-deposited multilayer structure of w-AlN/Ag, (b) the same after LA, and (c) the as-deposited multilayer structure of a-AlN/Ag and (d) the same after LA. LA fluence for all relevant samples in this figure was set at 600 mJ/cm².

After LA treatment, the upper part of the multilayer was highly affected. The multilayer structure is destroyed and the enlarged NPs are fairly homogenously distributed inside the AlN matrix, retaining a high density in the case of a-AlN. On the contrary, in the case of w-AlN only, the top of the laser treated part of the sample is affected and is generally depleted of Ag, indicating a higher diffusivity of Ag in w-AlN compared to a-AlN. The w-AlN/Ag presents a destruction of periodicity affecting only the top six Ag layers, while two more layers were partially destroyed. The sample thickness that retained a stratified arrangement is indicated by a dashed line in the inset of **Figure 10b**, which depicts the contrast intensity profile along the film thickness. In the case of a-AlN/Ag, this structural re-arrangement is more extensive as shown in **Figure 10d**, and it affected the top 10 Ag layers, while again 2 additional layers were partially affected.

The above considerations make AlN's thermal conductivity a crucial parameter in the LA process. k_{AlN} is sensitive to the deposition method and conditions and can show large variations ranging from about 10 W/mK for amorphous AlN [64] to 285 W/mK for single crystal [65]. To explore its effect, the temperature transient is plotted (at the top of the multilayer) for several different values of the AlN thermal conductivity. A significant difference depending on k_{AlN} is found for the peak temperature rise when the laser pulse is on, but it quickly diminishes afterwards. The most important effect of k_{AlN} is shown in the spatial distribution of the peak temperature rise plotted in **Figure 11(c)**. In particular, for high values of k_{AlN}, the temperature profile is almost constant across the multilayer, even though most of the laser fluence is absorbed within the first 100 nm, as shown in **Figure 11(a)**, where

Figure 11. (a) UV laser (193 nm) absorption profile in our model structure (21 5nmAg/10nmAlN bilayers on Si), (b) normalised temperature transient at the top of the multilayer for various values of k_{AlN}. The inset shows the pulse profile of the excimer laser, (c) the normalized peak-temperature spatial distribution for the corresponding cases of (b). Large gradients across the film are obtained for low values of k_{AlN}, (d) peak transient temperature distribution as a function of distance from the film's top surface, at different incident laser fluence assuming a nonlinear thermal conductivity for the multilayer structure (w-AlN and Ag). Solid lines are for the linear case (zero fluence limit) for w-AlN (k = 285 W/mK) and for an ultra-low conductance a-AlN (k = 10 W/mK), both for a linear Ag thermal conductivity of 429 W/mK. Broken lines are for nonlinear w-AlN and Ag for different laser fluence. In the inset we plot the experimental temperature dependent thermal conductivities of Ag [50] and w-AlN [48] assumed in this work.
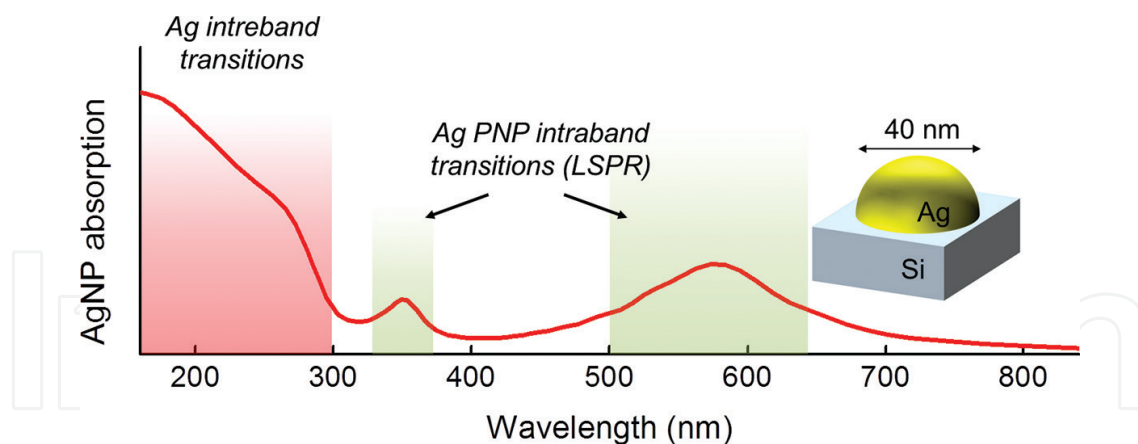
the spatial absorption profile within the multilayer is plotted. One can note that for low values of k_{AlN}, a significant temperature gradient is developed across the multilayer. Higher temperatures close to the surface and lower close to the substrate will result into different annealed structures, explaining our experimental results. It should be stressed here that up to now only the linear heat transport regime is studied in order to get insight into the temperature transients and gradients that can be developed and have not considered the thermodynamics of phase changes, e.g. melting and resolidification. Regarding radiation and convection losses from the top surface, a simple estimate suffices to show that they are of no consequence [20].

4. Surface nanostructuring

Plasmonic templates can be fabricated by LA of a thin metal film on a substrate, resulting into nanoparticle arrangements with many plasmonic applications as mentioned in Section 1 [11, 13, 14, 17, 19, 47–54]. The enabling property of these templates is the coherent surface plasmon oscillations excited by the incident light at specific frequencies, with high selectivity on the metal nanostructure size and shape. But a selective plasmon excitation is necessarily accompanied by selective light absorption, and thus by selective heating of the nanostructure. It is natural thus to allow this core property of the target application, to become itself one of the drivers in a multi-pulse laser induced self-assembly process. Besides heating, selective cooling is also an integral part of restructuring. But as the cooling rate depends on the geometric features of the nanostructure, a second driver for the self-assembly process is introduced. The available light absorption mechanisms in the case of nanostructured noble metals such as Ag, Au and Cu, can be generally split into (a) inter-band absorption from the metal's internal d-electrons, which is typically enabled at UV frequencies and in general is not size-dependent, and (b) resonant intra-band absorption, from the conduction electrons due to excitation of localized surface plasmon resonances (LSPR), which is strongly size and shape-selective. As an example, the overall absorption profile of an Ag nanoparticle (hemispherical shape) with diameter of 40 nm on top of a Si substrate is plotted in **Figure 12**, showing the spectral domains of the two absorption mechanisms. Utilization of these absorption modes combined with the size selectivity of cooling (~nanostructure surface/volume ratio) constitutes a toolbox for controlling the self-assembly of nanoparticles.

If after some laser treatment of a thin silver film on a Si substrate, Ag NPs with specific diameters have been formed, what will be the effect of a new incoming laser pulse? For this consideration, computer simulations can help explore the potential use of the various modes presented above. For computational simplicity a hexagonal lattice of Ag-hemispheres (40 nm in diameter) on a Si substrate with separation aspect ratios a/d = 1.2 (periodicity/diameter) have been assumed. First of all, **Figure 13a** shows the absorption per nm at different depths for this structure. The different modes relating to inter-band and intra-band absorptions in the nanoparticle, as well as the absorption in the substrate, are clearly shown. The absorption spatial distribution is then time-integrated with the appropriate laser temporal profile for each wavelength, depicted in **Figure 13c**. The experimentally acquired laser pulse
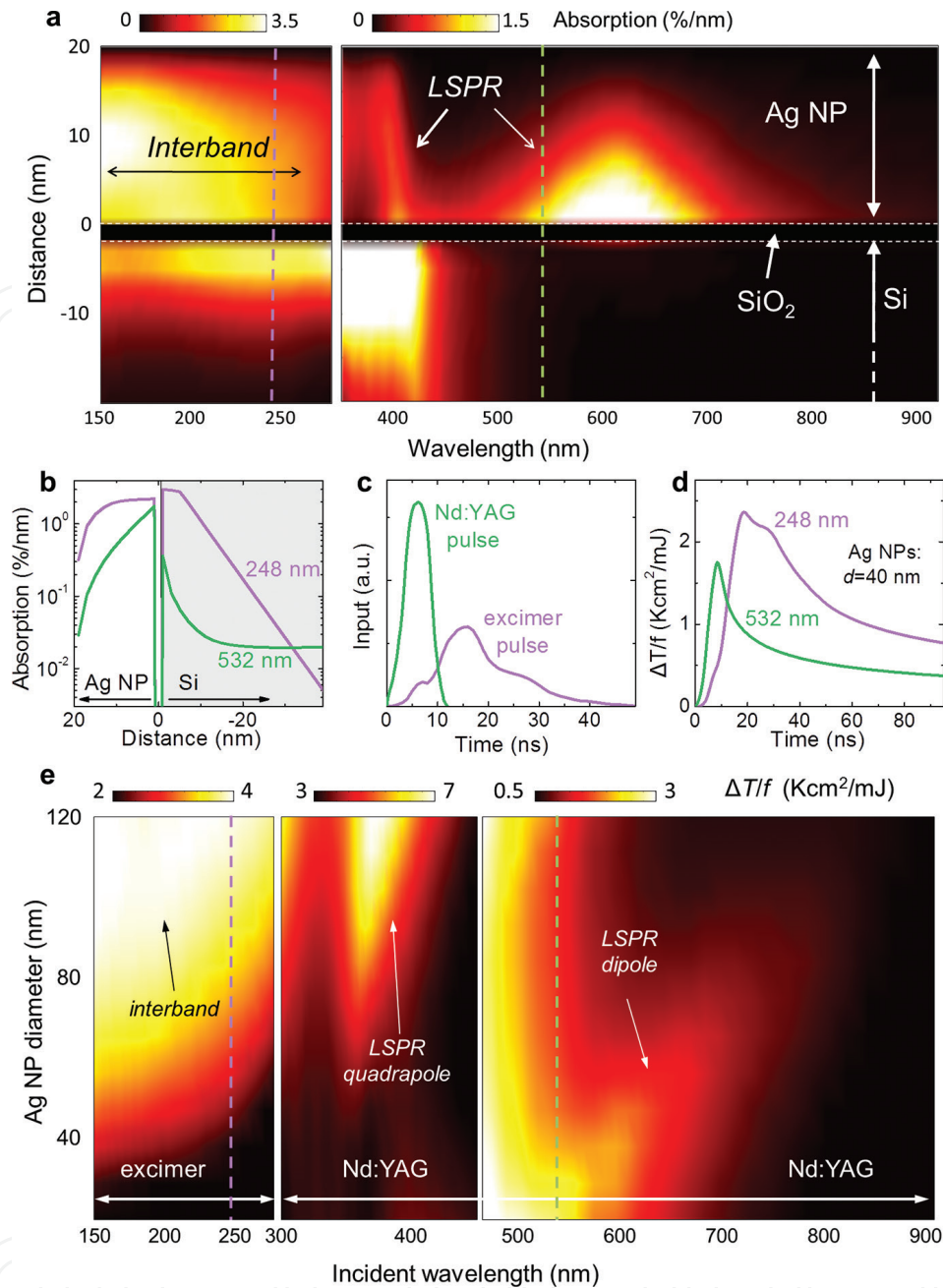
Figure 12. Simulated absorption spectrum of a 40 nm diameter Ag nanoparticle on top of a Si substrate. Inter-band absorption dominates the red shaded region, while LSPR driven absorption is dominating the green shaded regions (at ~350 nm the quadrupole 428 and ~580 nm the dipole contributions, respectively).

temporal profile from an excimer source was used for the 150–180nm range whereas the pulse temporal profile of a Nd:YAG source was used for the 300–900 nm range in a numeri‐ cal solution of the numerically 1D heat diffusion equation presented in Eq. (1). Thus, we get the temperature transient profile at every point in the structure in degrees/mJ of laser fluence. In **Figure 13d**, the temperature transients for the two primary wavelengths used in recent experimental studies are presented. This way the mapping of the maximum tempera‐ ture rise as a function of particle size, laser wavelength and laser fluence can be constructed. Bear in mind that the temperature transient follows the actual pulse temporal shape, but a significant transient tail also persists for longer times. The above discussion indicates that the processes discussed here are power and fluence dependent respectively, making the explicit time-dependent simulations essential. For a given laser fluence, direct information regarding particle heating can be extracted, and the probability of a nanoparticle melting or not can be assessed.
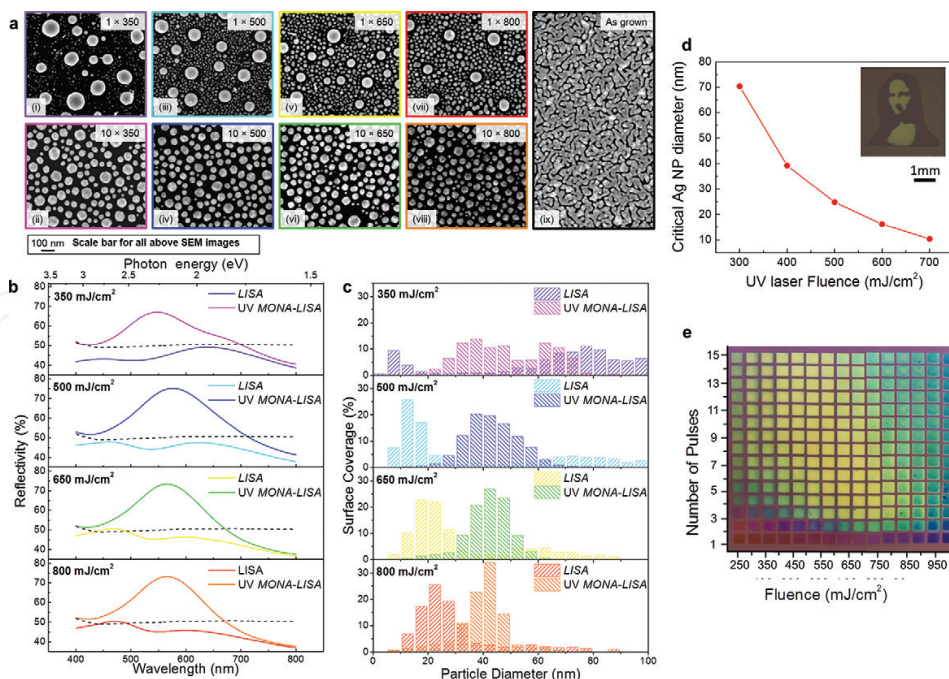
The global picture can then be revealed by considering how nanoparticle arrays of differ‐ ent sizes of nanoparticles behave to different wavelength illuminations. This is plotted in **Figure 13e**, showing the peak transient temperature, per unit of laser fluence, developed in the nanoparticle as a function of both the wavelength and the nanoparticle size. The dipole contribution is weaker than the contributions at shorter wavelengths (quadrupole LSPR and Si inter-band absorption), however, within a specific annealing plan one can always irradiate at one single wavelength, thus the strength of each band is of no importance other than defin‐ ing the fluence that each laser wavelength should be used. Upon melting and resolidification, a random distribution of sizes will emerge. However, repeated laser pulses at a particular wavelength will lead to the melting of one particular size group and thus to its eventual extinction. The main concept behind this approach is, thus, repeated laser treatment, target‐ ing different size groups with different laser wavelengths, driving the final size distribution towards a predetermined one. This process has been termed as 'modification of nanopar‐ ticles arrays by laser-induced self-assembly' (MONA-LISA) [47] and has been experimentally demonstrated.

Figure 13. (a) Vertical absorption (% per nm) profile for the 40 nm diameter Ag nanoparticle. Indicated with the two dashed lines are the two primary wavelengths used (248 and 532 nm). (b) Absorption percentage per nm profile in the model structure for the two wavelengths used. (c) Temporal profile of the two different laser sources. (d) Corresponding temperature transients developed in the Ag NP (normalized to the laser fluence). (e) Global map showing the peak temperature developed in an Ag NP on top of Si versus wavelength and NP size.

As a first step, a single shot UV LA process was utilised, to initialize nanoparticle formation from a semi-continuous metal thin film, by laser induced self-assembly (LISA). This resulted into the restructuring of the Ag thin film into nanoparticle arrangements in macroscopic scales (several mm²). The LISA process with a UV laser (248 nm) is strongly fluence-dependent as demonstrated by the SEM images of **Figure 14a**. The Ag NP size distributions are generally

Figure 14. (a) SEM images of samples processed with LISA (1 pulse, 248 nm LA) and UV MONA-LISA (10 pulses, 248 nm) under various applied fluences. (b) The effect of LISA and UV MONA-LISA on the optical reflectivity spectra of a 10 nm Ag thin film under various applied fluences. (c) Surface coverage of the nanoparticles in relation to the particle diameter for all the cases of (a). (d) Critical nanoparticle diameter (the diameter value under which every particle remains practically cold during the UV LA process, hence these particles cannot be further manipulated upon irradiation) as a function of applied laser fluence. Inset depicts a portrait of Da Vinci's Mona Lisa: a microscopic pattern engraved on silicon wafer in a single pixel processing using series of photolithographic masks. (e) A digital photo of a grid of LISA / UV MONA-LISA spots of varying fluence (*x*-axis) and number of pulses (*y*-axis) produced on a 10 nm Ag thin film.

bimodal, consisting of one set of coarse and one set of fine NPs. Increasing the laser fluence from 350 to 800 mJ/cm² resulted into a decreasing difference between the two NP sets, as shown by the quantified SEM images (**Figure 14c**, purple, cyan, yellow and red lines). The modification of NP assemblies by multiple laser pulses (MONA-LISA process) involves the utilization of the selective optical absorption and the heat dissipation, as presented in the theoretical approach above. For this consideration, the initial assemblies of NPs were subjected to a series of UV and/ or VIS LA steps.
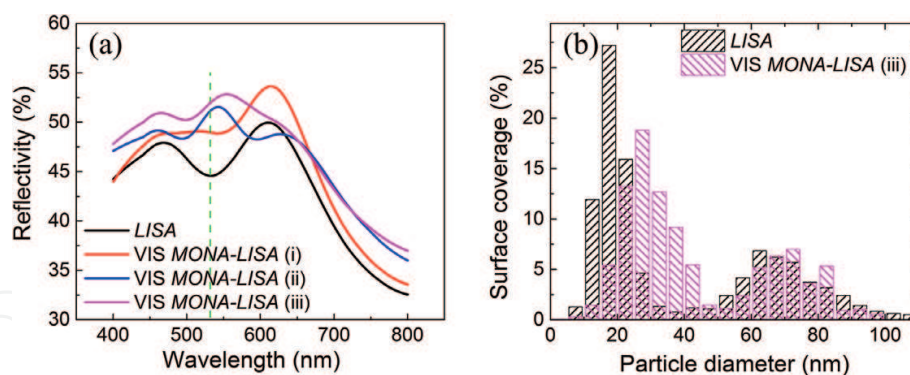
The case of UV MONA-LISA is first considered, i.e. processing by multiple UV (248 nm) laser pulses, and the effect of inter-band absorption is correlated with the size-selective heat dissipation. **Figure 14b** shows the optical reflectivity spectra of a 10 nm Ag film recorded after UV MONA-LISA applying 10 successive UV laser pulses at various fluences (magenta, blue, green and orange lines for 350, 500, 650 and 800 mJ/cm², respectively). Comparing these spectra with those from the previous LISA processing revealed that the consecutive pulses transform the two reflectivity peaks into one, indicating a gradual transformation of the bimodal distributions into unimodal ones. This was also confirmed by the corresponding SEM images and the size distribution histograms in **Figure 14a** and **c** (magenta, blue, green and orange bars), respectively. The reshaping of the particles is pre-

dominantly due to the disappearance of the larger particles. The physics behind that observation is based on the stronger heating of the larger NPs and faster heat dissipation from the finer NPs due to their higher effective surface (surface to volume ratio). As a result, the finer nanoparticles remain cold during UV MONA-LISA. To quantify this, photothermal calculations [47] were employed, in order to determine the equitemperature contour lines vs. nanoparticle diameter, from which the critical size under which the particles remain practically cold during the UV MONA-LISA. Considering the bulk Ag melting point of 960°C, the calculated values of the critical diameter vs. the laser fluence (248 nm) are displayed in **Figure 14d**. We remark that the critical diameter is highly dependent on the thermal conductivity of the substrate; less thermally conductive substrate would hinder heat dissipation. The UV MONA-LISA process is thus based on the ability of the larger particles to raise their temperature above their melting point, and consequently re-solidifying forming smaller particles with a stochastic size distribution, while the smaller ones remain below the melting threshold and therefore remain practically unaffected. As a result, successive pulses suppress the population of the coarse particles, gradually transforming them to finer particles via stochastic size redistribution. The wide range of size distributions achieved by LISA and UV MONA-LISA results in a vast colour palette of plasmonic responses as those presented in **Figure 14e** (real visual appearance of the Ag nanoparticle assemblies). Combining LISA and MONA-LISA process with projection masks enables the production of multicolour images of high spatial resolution and colour contrast. Such an example is presented in the inset of **Figure 14d**, depicting the portrait of Da-Vinci's famous 'Mona Lisa'.

The implementation of MONA-LISA employing exclusively UV pulses has the inherent limitation of the UV absorption being rather insensitive to nanoparticle size, and as a result, the size selectivity of the process is based exclusively on the size selectivity of the heat dissipation. Thus, only the large particles are affected by the successive laser pulses. Finer particles can be further manipulated by exploiting their selective optical absorption via LSPR using a visible wavelength, resulting in larger optical absorption and hence higher temperature rise, as predicted by the computational results presented in **Figure 13**. The optimal condition of narrowing the LSPR bandwidth at 532 nm was achieved by applying 500 pulses at 125 mJ/ cm^2, which shows that the VIS MONA-LISA is slower compared to the UV MONA-LISA that reached at steady state at 10 pulses. This is well expected considering the computational results of **Figure 13**, where a lower temperature rise is evident at visible wavelengths compared to UV processing.

Exploring the VIS MONA-LISA one can start from a UV MONA-LISA process (248 nm, 2 pulses at 350 mJ/cm^2) which demonstrates a double reflectance peak (due to bimodal nanostructuring) notably with no particular response close to 532 nm, as shown in **Figure 15a** (black line). Applying, VIS MONA-LISA to this area, with 500 pulses (i), 2000 pulses (ii) and 4000 pulses (iii) results in gradually re-adjusting the bimodal distribution to one with a peak very close to the laser processing wavelength (532 nm). The corresponding SEM images are shown in Ref. [47]. Analysis of these SEM images results in the histograms of **Figure 15b**. It is noteworthy that the VIS MONA-LISA probes particularly the finer Ag nanoparticles (<20 nm) confirming the computational analysis presented in **Figure 13**.

Figure 15. (a) Optical reflectivity spectra of LISA (2 pulse, 248 nm at 350 mJ/cm² - black line), used as a template for the subsequent Visible MONA-LISA (500 pulses (red line), 2000 pulses (blue line) and 4000 pulses (magenta line), 532 nm at 125 mJ/cm²). The green dashed line sets the 532 nm mark. (b) Surface coverage of the nanoparticles in relation to the particle diameter for each laser treatment of (a).

5. Conclusions

Functional plasmonic templates can be fabricated by LA. In particular, two distinct cases have been discussed: laser nanostructuring of either ceramic/metal multilayers and composites or ultra-thin metal films results on sub-surface or surface plasmonic patterns, respectively, with many potential applications.

Theoretical investigations have highlighted the underline physics of laser-induced sub-surface and surface plasmonic nanostructuring: the absorption profile of the film and the temperature spatial distribution strongly depend on the structure parameters such as the metal volume ratio, the total thickness of the film and the thermal conductivity of the dielectric. By properly designing these parameters, combined with tuning the LA conditions (wavelength, number of pulses and fluence) one can arrive at plasmonic templates with predetermined morphology and optical response. The latter was demonstrated in experiments in which either AlN:Ag nanocomposites or multilayers of alternative AlN/Ag layers were subjected in UV LA leading to a sub-surface formation of PNPs sealed in an AlN matrix with a localized surface plasmon resonance response.

An extensive experimental and theoretical investigation has highlighted the photothermal processes involved in laser-induced surface plasmonic nanostructuring. Specifically, templates consisting of hemi-spherical Ag PNPs on Si substrate, with different arrangements and sizes, for both UV and optical irradiation have been explored. Different absorption mechanisms, which are size selective and enable geometric specificity, have been identified: (a) inter-band absorption taking place at the UV zone, probing the metal's internal d-electrons and (b) intra-band absorption taking place at the near-UV, and visible zone, probing the metal's free electrons at the specific spectral position of LSPR. In particular, by sequentially tuning the laser wavelength into resonance with different physical absorptions, we can selectively target the melting and re-solidification of different particle size groups. This process was termed: "modification of nanoparticle arrays by laser-induced self-assembly" (MONA-LISA).

Acknowledgements

Author details

Nikolaos Kalfagiannis[1]*, Demosthenes C. Koutsogeorgis[1], Elefterios Lidorikis[2] and Panos Patsalas[3]

*Address all correspondence to: nikolaos.kalfagiannis@ntu.ac.uk

1 School of Science and Technology, Nottingham Trent University, Nottingham, United Kingdom

2 Department of Materials Science and Engineering, University of Ioannina, Ioannina, Greece

3 Department of Physics, Aristotle University of Thessaloniki, Thessaloniki, Greece

References

[1] N. Lagos, M. M. Sigalas, E. Lidorikis. Theory of plasmonic near-field enhanced absorption in solar cells. Applied Physics Letters. 2011;**99**:063304.

[2] N. Kalfagiannis, P. G. Karagiannidis, C. Pitsalidis, N. T. Panagiotopoulos, C. Gravalidis, S. Kassavetis, P. Patsalas, S. Logothetidis. Plasmonic silver nanoparticles for improved organic solar cells. Solar Energy Materials and Solar Cells. 2012;**104**:165-174.

[3] H. A. Atwater, A. Polman. Plasmonics for improved photovoltaic devices. Nature Materials. 2010;**9**:205-213.

[4] M. J. Beliatis, S. J. Henley, S. Han, K. Gandhi, A. A. D. T. Adikaari, E. Stratakis, E. Kymakis, S. R. P. Silva. Organic solar cells with plasmonic layers formed by laser nanofabrication. Physical Chemistry Chemical Physics. 2013;**15**:8237-8244.

[5] H. Zoubos, L. E. Koutsokeras, D. F. Anagnostopoulos, E. Lidorikis, S. A. Kalogirou, A. R. Wildes, P. C. Kelires, P. Patsalas. Broadband optical absorption of amorphous carbon/

Ag nanocomposite films and its potential for solar harvesting applications. Solar Energy Materials and Solar Cells. 2013;**117**:350-356.

[6]   P. Nikolaou, C. Mina, M. Constantinou, L.E. Koutsokeras, G. Constantinides, E. Lidorikis, A. Avgeropoulos, P.C. Kelires, P. Patsalas. Functionally graded poly(dimethylsiloxane)/ silver nanocomposites with tailored broadband optical absorption. Thin Solid Films. 2015;**581**:14-19.

[7]   E. Lidorikis. Modeling of enhanced absorption and Raman scattering caused by plasmonic nanoparticle near fields. Journal of Quantitative Spectroscopy and Radiative Transfer. 2012;**113**:2573-2584.

[8]   M. Moskovits. Surface-enhanced spectroscopy. Reviews of Modern Physics. 1985;**57**:783-826.

[9]   K. Kneipp, Y. Wang, H. Kneipp, L. T. Perelman, I. Itzkan, R. R. Dasari, M. S. Feld. Single molecule detection using surface-enhanced raman scattering (SERS). Physical Review Letters. 1997;**78**(9):1667.

[10] Y. Fang, N. H. Seong, D. D. Dlott. Measurement of the distribution of site enhancements in surface-enhanced Raman scattering. Science. 2008;**321**:388-392.

[11] S. J. Henley, J. D. Carey, S. R. P. Silva. Laser-nanostructured Ag films as substrates for surface-enhanced Raman spectroscopy. Applied Physics Letters. 2006;**88**:081904.

[12] S. J. Henley, S. R. P. Silva. Laser direct write of silver nanoparticles from solution onto glass substrates for surface-enhanced Raman spectroscopy. Applied Physics Letters. 2007;**91**:023107.

[13] K. Christou, I. Knorr, J. Ihlemann, H. Wackerbarth, V. Beushausen. Fabrication and characterization of homogeneous surface-enhanced Raman scattering substrates by single pulse UV-laser treatment of gold and silver films. Langmuir. 2010;**26**(23):18564-18569.

[14] C. H. Lin, L. Jiang, J. Zhou, H. Xiao, S. J. Chen, H. L Tsai. Laser-treated substrate with nanoparticles for surface-enhanced Raman scattering. Optics Letters. 2010;**35**(7):941-943.

[15] J. Chen, C. Glaus, R. Laforest, Q. Zhang, M. Yang, M. Gidding, M. J. Welch, Y. Xia. Gold nanocages as photothermal transducers for cancer treatment. Small. 2010;**6**:811-817.

[16] C. Ayala-Orozco, C. Urban, M. W. Knight, A. S. Urban, O. Neumann, S. W. Bishnoi, S. Mukherjee, A. M. Goodman, H. Charron, T. Mitchell, M. Shea, R. Roy, S. Nanda, R. Schiff, N. J. Halas, A. Joshi. Au nanomatryoshkas as efficient near-infrared photothermal transducers for cancer treatment: benchmarking against nanoshells. ACS Nano. 2014;**8**:6372-6381.

[17] A. Siozios, N. Kalfagiannis, D. V. Bellas, C. Bazioti, G.P. Dimitrakopulos, G. Vourlias, W.M. Cranton, E. Lidorikis, D. C. Koutsogeorgis, P. Patsalas. Sub-surface laser nanostructuring in stratified metal/dielectric media: a versatile platform towards flexible, durable and large-scale plasmonic writing. Nanotechnology. 2015;**26**:155301.

[18] C. Bazioti, G. P. Dimitrakopulos, T. Kehagias, P. Komninou, A. Siozios, E. Lidorikis, D. C. Koutsogeorgis, P. Patsalas. Influence of laser annealing on the structural properties of sputtered AlN: Ag plasmonic nanocomposites. Journal of Materials Science. 2014;**49**:3996-4006.

[19] A. Siozios, D. C. Koutsogeorgis, E. Lidorikis, G. P. Dimitrakopulos, T. Kehagias, H. Zoubos, P. Komninou, W. M. Cranton, C. Kosmidis, P. Patsalas. Optical encoding by plasmon-based patterning: hard and inorganic materials become photosensitive. Nano Letters. 2012;**12**:259-263.

[20] A. Siozios, D. C. Koutsogeorgis, E. Lidorikis, G. P. Dimitrakopulos, N. Pliatsikas, G. Vourlias, T. Kehagias, P. Komninou, W. Cranton, C. Kosmidis, P. Patsalas. Laser-matter interactions, phase changes and diffusion phenomena during laser annealing of plasmonic AlN: Ag templates and their applications in optical encoding. Journal of Physics D: Applied Physics. 2015;**48**:285306.

[21] C. F. Bohren, D. R. Huffman. Absorption and scattering of light by small particles. Wiley Interscience, New York; 1983.

[22] M. Rycenga, C. M. Cobley, J. Zeng, W. Li, C. H. Moran, Q. Zhang, D. Qin, Y. Xia. Controlling the synthesis and assembly of silver nanostructures for plasmonic applications. Chemical Reviews. 2011;**111**:3669-3712.

[23] S. A. Maier. Plasmonics: fundamentals and applications. Springer, New York; 2007.

[24] U. Kreibig, M. Vollmer. Optical properties of metal clusters. Springer, Berlin; 1995.

[25] N. J. Halas. Plasmonics: an emerging field fostered by Nano Letters. Nano Letters. 2010;**10**:3816-3822.

[26] M. L. Brongersma, V. M. Shalaev. The case for plasmonics. Science. 2010;**328**:440-441.

[27] E. Ozbay. Plasmonics: merging photonics and electronics at nanoscale dimensions. Science. 2006;**311**:189-193.

[28] K. S. Lee, M. A. J. El-Sayed. Gold and silver nanoparticles in sensing and imaging: sensitivity of plasmon response to size. Journal of Physical Chemistry B. 2006;**110**:19220-19225.

[29] M. M. Miller, A. A. Lazarides. Sensitivity of metal nanoparticle surface plasmon resonance to the dielectric environment. Journal of Physical Chemistry B. 2005;**109**:21556-21565.

[30] O. Kvitek, J. Siegel, V. Hnatowicz, V. Svorcik. Noble metal nanostructures: influence of structure and environment on their optical properties. Journal of Nanomaterials. 2013;**2013**:743684.

[31] M. R. Jones, K. D. Osberg, R. J. Macfarlane, M. R. Langille, C. A. Mirkin. Templated techniques for the synthesis and assembly of plasmonic nanostructures. Chemical Reviews. 2011;**111**:3736-3827.

[32] X. Lu, M. Rycenga, S. E. Skrabalak, B. J Wiley, Y. Xia. Chemical synthesis of novel plasmonic nanoparticles. Annual Reviews of Physical Chemistry. 2009;**60**:167-192.

[33] G. Walters, I. P. Parkin. The incorporation of noble metal nanoparticles into host matrix thin films: synthesis, characterisation and applications. Journal of Materials Chemistry. 2009;**19**:574-590.

[34] L. Armelao, D. Barreca, G. Bottaro, A. Gasparotto, S. Gross, C. Maragnob, E. Tondello. Recent trends on nanocomposites based on Cu, Ag and Au clusters: a closer look. Coordination Chemistry Reviews. 2006;**250**:1294-1314.

[35] J. H. Seo, J. H. Park, S. I. Kim, B. J. Park, Z. Ma, J. Choi, B. K. Ju. Nanopatterning by laser interference lithography: applications to optical devices. Journal of Nanoscience and Nanotechnology. 2014;**14**:1521-1532.

[36] U. Guler, J. C. Ndukaife, G. V. Naik, A. G. A. Nnanna, A. V. Kildishev, V. M. Shalaev, A. Boltasseva. Local heating with lithographically fabricated plasmonic titanium nitride nanoparticles. Nano Letters. 2013;**13**:6078-6083.

[37] G. Bracher, K. Schraml, M. Ossiander, S. Frédérick, J. J. Finley, M. Kaniber. Optical study of lithographically defined, subwavelength plasmonic wires and their coupling to embedded quantum emitters. Nanotechnology. 2014;**25**:075203.

[38] J. Toudert, D. Babonneau, S. Camelio, T. Girardeau, F. Yubero, J. P. Espinós, A. R. Gonzalez-Elipe. Using ion beams to tune the nanostructure and optical response of co-deposited Ag:BN thin films. Journal of Physics D: Applied Physics. 2007;**40**:4614-4620.

[39] V. A. Sivakov, K. Höflich, M. Becker, A. Berger, T. Stelzner, K. E. Elers, V. Pore, M. Ritala, S. H. Christiansen. Silver coated platinum core–shell nanostructures on etched Si nanowires: atomic layer deposition (ALD) processing and application in SERS. ChemPhysChem. 2010;**11**:1995-2000.

[40] Y. Lu, J. Y. Huang, C. Wang, S. Sun, J. Lou. Cold welding of ultrathin gold nanowires. Nature Nanotechnology. 2010;**5**:218-224.

[41] Y. K. Mishra, S. Mohapatra, D. Kabiraj, B. Mohanta, N. P. Lalla, J.C. Pivin, D. K. Avasthi. Synthesis and characterization of Ag nanoparticles in silica matrix by atom beam sputtering. Scripta Materialia. 2007;**56**:629-632.

[42] I. Tanahashi, Y. Manabe, T. Tohda, S. Sasaki, A. Nakamura. Optical nonlinearities of Au/SiO$_2$ composite thin films prepared by a sputtering method. Journal of Applied Physics. 1996;**79**:1244-1249.

[43] D. Lin, H. Tao, J. Trevino, J. P. Mondia, D. L. Kaplan, F. G. Omenetto, L. Dal Negro. Direct transfer of subwavelength plasmonic nanostructures on bioactive silk films. Advanced Materials. 2012;**24**:6088-6093.

[44] P. Nielsen, P. Morgen, A. C. Simonsen, O. Albrektsen. Hemispherical shell nanostructures from metal-stripped embossed alumina on aluminum templates. Journal of Physical Chemistry C. 2011;**115**:5552-5560.

[45] J. H. Park, P. Nagpal, K. M. McPeak, N. C. Lindquist, S. H. Oh, D. J. Norris. Fabrication of smooth patterned structures of refractory metals, semiconductors, and oxides via template stripping. ACS Applied Materials and Interfaces. 2013;**5**:9701-9708.

[46] P. Farzinpour, A. Sundar, K. D. Gilroy, Z. E. Eskin, R. A. Hughes, S. Neretina. Dynamic templating: a large area processing route for the assembly of periodic arrays of sub-micrometer and nanoscale structures. Nanoscale. 2013;**5**:1929-1938.

[47] N. Kalfagiannis, A. Siozios, D. V. Bellas, D. Toliopoulos, L. Bowen, N. Pliatsikas, W. M Cranton, C. Kosmidis, D. C. Koutsogeorgis, E. Lidorikis, P. Patsalas. Selective modification of nanoparticle arrays by laser-induced self assembly (MONA-LISA): putting control into bottom-up plasmonic nanostructuring. Nanoscale. 2016;**8**:8236-8244.

[48] M. J. Beliatis, S. J. Henley, S. R. P. Silva. Engineering the plasmon resonance of large area bimetallic nanoparticle films by laser nanostructuring for chemical sensors. Optics Letters. 2011;**36**(8):1362-1364.

[49] C. Favazza, R. Kalyanaraman, R. Sureshkumar. Robust nanopatterning by laser-induced dewetting of metal nanofilms. Nanotechnology. 2006;**17**:4229-4234.

[50] H. Krishna, N. Shirato, C. Favazza, R. Kalyanaraman. Pulsed laser induced self-organization by dewetting of metallic films. Journal of Materials Research. 2011;**26**(2):154-169.

[51] C. E. Rodrígueza, R. J. Peláeza, C. N. Afonsoa, S. Riedelb, P. Leidererb, D. Jimenez-Reyc, A. Climent-Fontc. Plasmonic response and transformation mechanism upon single laser exposure of metal discontinuous films. Applied Surface Science. 2014;**302**:32-36.

[52] F. Ruffino, A. Pugliara, E. Carria, C. Bongiorno, C. Spinella, M. G. Grimaldi. Formation of nanoparticles from laser irradiated Au thin film on SiO_2/Si: elucidating the Rayleigh-instability role. Materials Letters. 2012;**84**:27-30.

[53] F. Ruffino, E. Carria, S. Kimiagar, I. Crupi, F. Simone, M. G. Grimaldi. Formation and evolution of nanoscale metal structures on ITO surface by nanosecond laser irradiations of thin Au and Ag films. Science of Advanced Materials. 2012;**4**:708-718.

[54] J. Trice, D. Thomas, C. Favazza, R. Sureshkumar, R. Kalyanaraman. Pulsed-laser-induced dewetting in nanoscopic metal films: theory and experiments. Physical Review B. 2007;**75**:235439.

[55] Ch. E. Lekka, P. Patsalas, Ph. Komninou, G. A. Evangelakis. Electronic properties and bonding characteristics of AlN:Ag thin film nanocomposites. Journal of Applied Physics. 2011;**109**:054310.

[56] P. Lautenschlager, M. Garriga, L. Viña, M. Cardona. Temperature dependence of the dielectric function and interband critical points in silicon. Physical Review B. 1987;**36**:4821-4830.

[57] P. L. Redmond, A. J. Hallock, L. E. Brus. Electrochemical Ostwald ripening of colloidal Ag particles on conductive substrates. Nano Letters. 2005;**5**:131-135.

[58] A. Lotsari, G. P. Dimitrakopulos, T. Kehagias, P. Kavouras, H. Zoubos, L. E. Koutsokeras, P. Patsalas, Ph. Komninou. Structure, stability and mechanical performance of AlN:Ag nanocomposite films. Surface and Coatings Technology. 2010;**204**:1937-1941.

[59] G. M. Matenoglou, H. Zoubos, A. Lotsari, C.E. Lekka, Ph. Komninou, G. P. Dimitrakopulos, C. Kosmidis, G. A. Evangelakis, P. Patsalas. Metal-containing amorphous carbon (a-C:Ag) and AlN (AlN:Ag) metallo-dielectric nanocomposites. Thin Solid Films. 2009;**518**:1508-1511.

[60] A. Siozios, H. Zoubos, N. Pliatsikas, D. C. Koutsogeorgis, G. Vourlias, E. Pavlidou, W. Cranton, P. Patsalas. Growth and annealing strategies to control the microstructure of AlN:Ag nanocomposite films for plasmonic applications. Surface and Coatings Technology. 2014;**255**:28-36.

[61] J. D. Jackson. Classical electrodynamics. 3rd ed. Wiley, New York; 1999.

[62] E. Lidorikis, S. Egusa, J. D. Joannopoulos. Effective medium properties and photonic crystal superstructures of metallic nanoparticle arrays. Journal of Applied Physics. 2007;**101**:054304.

[63] R. Donald, L. E. S. Pitts. Schaum's outline of theory and problems of heat transfer. McGraw-Hill, New York; 1998.

[64] C. Duquenne, M. P. Besland, P. Y. Tessier, E. Gautron, Y. Scudeller, D. Averty. Thermal conductivity of aluminium nitride thin films prepared by reactive magnetron sputtering. Journal of Physics D: Applied Physics. 2012;**45**:015301.

[65] G. A. Slack, R. A. Tanzilli, R. O. Pohl, J. W. Vandersande. The intrinsic thermal conductivity of AlN. Journal of Physics and Chemistry of Solids. 1987;**46**:641-647.